

The Allosteric Switching Mechanism in Bacteriophage MS2

Matthew R. Perkett¹ and Michael F. Hagan^{1, a)}

Martin Fisher School of Physics, Brandeis University, Waltham, MA, USA

In this article we use all-atom simulations to elucidate the mechanisms underlying conformational switching and allostery within the coat protein of the bacteriophage MS2. Assembly of most icosahedral virus capsids requires that the capsid protein adopt different conformations at precise locations within the capsid. It has been shown that a 19 nucleotide stem loop (TR) from the MS2 genome acts as an allosteric effector, guiding conformational switching of the coat protein during capsid assembly. Since the principal conformational changes occur far from the TR binding site, it is important to understand the molecular mechanism underlying this allosteric communication. To this end, we use all-atom simulations with explicit water combined with a path sampling technique to sample the MS2 coat protein conformational transition, in the presence and absence of TR-binding. The calculations find that TR binding strongly alters the transition free energy profile, leading to a switch in the favored conformation. We discuss changes in molecular interactions responsible for this shift. We then identify networks of amino acids with correlated motions and side chain conformations to reveal the mechanism by which effects of TR binding span the protein. The analysis predicts amino acids whose substitution by mutagenesis could alter populations of the conformational substates or their transition rates.

I. INTRODUCTION

The controlled interconversion between protein conformational states is crucial for essential cellular functions, including signaling, metabolism, and assembly of the dynamic cytoskeleton. A key regulatory role in such processes is often played by allosteric effectors, whose binding favors a particular protein conformation. The transition pathways by which proteins interconvert between these folded states are largely unknown because intermediates along the pathways cannot be directly characterized by experiments. Similarly, it remains poorly understood how perturbations due to effector binding are communicated across the protein to alter its conformational free energy landscape. In this article we combine long unbiased all-atom molecular dynamics (MD) simulations, an efficient pathway sampling algorithm called the string method¹⁻⁹, and analysis of inter-residue correlations to characterize a protein conformational transition pathway and how it is affected by effector binding. In particular, we study the conformational transition of the MS2 coat protein dimer, and how the binding of an RNA stem loop from the MS2 genome acts as a molecular conformational switch that guides protein assembly into an icosahedral capsid.

MS2 is a small bacteriophage that infects male *E. Coli*. During virus assembly, 180 copies of the coat protein (CP) spontaneously assemble around a 3,569 nucleotide single-stranded RNA genome to form an icosahedral capsid. The capsid is a $T=3$ structure, meaning that the CPs adopt three conformations (termed A,B,C) which are precisely arranged within the capsid¹⁰. Major structural differences among the protein conformations are confined to the FG loop, which in the A and C conformations forms an anti-parallel β -hairpin, but in the B conformation is a

flexible loop pulled back against the dimer with a small α -helix kink. The A and C monomers are thus nearly identical, and their FG loops meet at 20 3-fold (quasi-6-fold) axes, whereas the FG loops of the B monomers meet at the 12 5-fold interfaces. In solution, the monomers form stable, non-covalent dimers, which are the basic assembly subunits and will be denoted as CP₂ (Fig. 1 b,c). Formation of the capsid thus requires that 30 CC and 60 AB dimers associate and arrange themselves into the icosahedral geometry (Fig. 1 a).

Based on structural studies, *in vitro* assembly assays, and modeling, it has been proposed that allosteric interactions between CP₂ and the viral genome guide conformational selection during MS2 assembly¹²⁻¹⁵. Capsid assembly can be triggered *in vitro* by the addition of a 19-nucleotide RNA stem-loop (TR) fragment from the genome. TR encompasses the start codon for the replicase protein, and has been shown to bind strongly to the bottom of CP₂^{16,17}. In the crystal structure, TR is bound to the CC dimers in two symmetric orientations, while steric constraints allow only a single orientation for the AB dimer (Fig. 1 g,h).

In vitro experiments by Stockley and coworkers¹² on wild-type CP showed that, in the absence of genomic RNA, CP assembles slowly and produces only a low yield of capsids. Adding a molar ratio of TR results in a strongly bonded CP₂:TR complex that is kinetically trapped. However, adding an equal molar ratio of CP₂ to CP₂:TR results in rapid and efficient assembly. Furthermore, NMR studies on an assembly-incompetent mutant MS2 coat protein (W82R), showed that TR binding induces a conformation change from a symmetric dimer (presumably BB-like) to an asymmetric dimer (presumably AB-like). Based on these observations, it was proposed that during assembly of wild-type (WT) MS2 capsid proteins, TR binding acts as a molecular switch which favors a conformational change from the symmetric CC dimer to the asymmetric AB dimer¹². Since both AB and CC dimers are needed for efficient assembly, this scenario

^{a)}Electronic mail: hagan@brandeis.edu

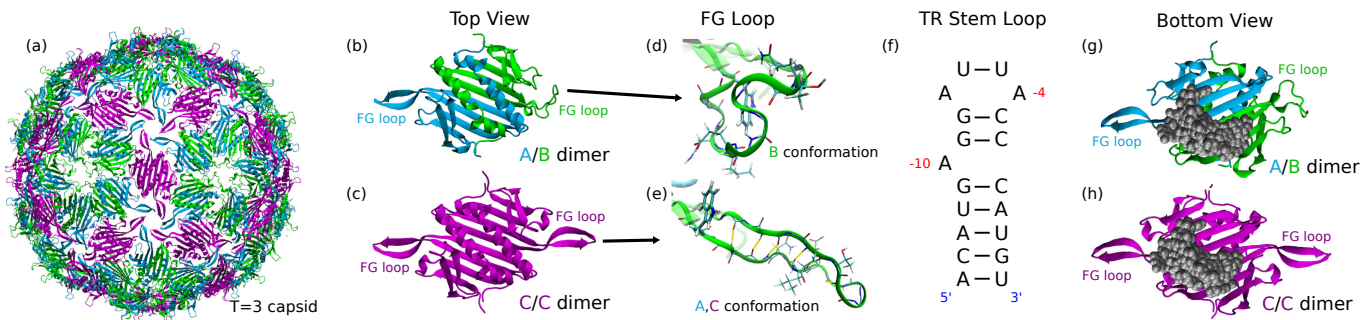


FIG. 1. MS2 Capsid geometry and subunit structure. (a) The complete T=3 MS2 capsid of 27.5nm diameter is comprised of 30 CC and 60 AB dimers. It has icosahedral symmetry with the 5-fold vertices as AB dimers and the 3-fold vertices as 3 AB + 3 CC dimers. (pdb ID: 1BMS) (b)-(c) the AB and CC dimers (respectively) colored according to their conformation. The B conformation differs significantly from the A and C conformations in the FG loop. (d)-(e) A close up view of the FG loop with a selection of side chains shown as bonds. The B conformation lacks the hydrogen bonds found in the A and C conformations (and shown in yellow). (f) The nucleic acid sequence of the TR stem loop, which binds with high affinity to the base of the MS2 dimer. The sequence positions of the adenines that bind most strongly are labeled in red (-10 and -4). (g)-(h) MS2 AB and CC dimers shown with the RNA stem loop (TR) bound to their base (pdb ID: 2BU1¹¹). The RNA can adopt two symmetric positions for the CC dimer (only one shown), but the AB dimer allows only one position due to steric collisions. The RNA is shown as grey VDW spheres.

is consistent with the observation that pure solutions of either CP₂ (assumed to be CC) or CP₂:TR (assumed to be AB:TR) are kinetically trapped whereas an equal molar ratio of CP₂ to CP₂:TR results in rapid and efficient assembly. Subsequent theoretical models suggest that such a conformational switch is consistent with existing structural data and assembly kinetics^{13-15,18}.

Since TR binds CP₂¹⁷ (Fig. 1 g,h) about 12 Å from the FG loop where the conformation change is localized, there is great interest in understanding the molecular mechanism underlying the apparent allosteric communication between these two regions of the protein. Using all-atom normal mode analysis, Dykeman et al.¹³ found that TR binding to an initially symmetric CC conformation leads to asymmetries consistent with the AB conformation. Namely, fluctuations of residues near the FG loop on the A* chain (meaning the chain that corresponds to the A chain in the AB dimer conformation) are suppressed, whereas those near the B* FG loop increase.

The goal of this paper is to directly calculate the MS2 capsid protein conformational free energy landscape, to learn how it is altered by the binding of the genome fragment TR, and to elucidate the molecular basis by which perturbations caused by TR binding are communicated across the protein. To this end, we employ the string method¹⁻⁵ to identify and characterize the most probable transition pathways and associated free energy profiles for the conformational transition in the presence and absence of TR, using all-atom simulations with explicit water. Furthermore, to directly probe the molecular basis for allosteric communication, we characterize correlations of amino acid conformational statistics and motions within long, unbiased MD simulation trajectories. These combined calculations demonstrate that the conformational transition is a complex, multi-step pro-

cess with multiple metastable minima, and is stabilized by multiple molecular-scale interactions whose statistics can be altered by molecular binding in disparate regions of the protein. The analysis predicts several amino acids whose substitution by mutagenesis could alter populations of the conformational substates or their transition rates. These findings may shed light on the mechanisms by which molecular binding affects conformational free energy landscapes in a wide variety of proteins, as well as for understanding the diverse roles of RNA in viral assembly.

Previous computational works have used enhanced sampling methods to examine the effect of small molecule substrates on protein interconversion pathways and free energies, with a particular focus on the enzyme adenylylate kinase¹⁹⁻²³. Here, we perform such an analysis to understand the effect of an RNA fragment on conformational interconversion of a viral protein which plays a key role in the capsid assembly process. We then analyze the effect of RNA binding on the motions and conformational statistics of amino acids within the stable substates. By relating these fluctuations within the free energy basins to differences between the high free energy transition pathways in the presence and absence of bound RNA, we elucidate the mechanisms underlying allosteric influence of protein conformations.

This article is arranged as follows. In section II we describe the model, simulations, and methodologies used to sample the transition. In section III, we describe the transition pathways predicted by the string method in the presence and absence of TR, we highlight some residues found to play key roles in stabilizing the transition based on the converged strings and long unbiased MD simulations, and we present results of mutual information and covariance analysis on correlations between

amino acid conformations and motions. Finally, in section IV we discuss implications of these results for understanding the mechanism underlying the conformational transition and how it is influenced by TR binding. Additional methodological details are given in the appendices.

II. METHODS

A. Systems and simulations

Systems. For statistical analysis and for generating beginning and end points for string method calculations, we initialized unbiased MD simulations from two MS2 capsid protein dimer conformations, each in the presence and absence of the RNA stem loop TR. We denote the four systems as AB, CC, AB:TR, and CC:TR. To avoid complications associated with the fact that P78 undergoes a *cis* to *trans* switch between conformations, we studied P78N mutants, which assemble complete capsids but are not infectious²⁴. The AB and CC dimer structures were therefore extracted from a crystal structure of the empty P78N capsid (pdb ID 1BMS²⁵). Since no crystal structure for P78N capsids with TR is available, we extracted AB:TR and CC:TR from a wild type MS2 capsid containing TR (pdbid 2BU1), and performed the P78N mutation in silico using VMD²⁶. The first and last bases in the RNA stem loop (A and U) for 2BU1 are missing, and were added using CHARMM²⁷.

Each of the four dimer structures was solvated with at least 1nm of water on each side of the structure. The resulting simulation boxes were approximately 10.2nm x 7.7nm x 5.6nm for CP₂ and 10.6nm x 7.2nm x 7.5nm for CP₂:TR. We ensured that each pair of systems intended to serve as beginning and end points of the same string (AB, CC) and (AB:TR, CC:TR) had the same number of atoms. Water molecules were replaced at random with Na⁺ and Cl⁻ ions to neutralize the charge and to bring the ionic strength to 0.1M. The total system size was approximately 41,000 atoms for CP₂ and 58,000 atoms for CP₂:TR. During equilibration, an orientation restraint was added to keep the dimer from self-interaction across the periodic boundary. For long unbiased MD calculations, larger water boxes (approximately 10.2nm³ for both CP₂ and CP₂:TR) were used with no orientation restraints. Details about the equilibration protocol are given in appendix A 1.

Simulations. Simulations were performed with version 4.5.5 of Gromacs²⁸ modified with version 1.3.0 of the plugin PLUMED²⁹, which was used to generate all restraints and monitor collective variables. The CHARMM27 all-atom forcefield³⁰ including the CMAP correction³¹ was used to represent protein atoms and the TIP3P model^{32,33} was used for water molecules. Bond lengths were constrained using the LINCS algorithm³⁴ with order 4. The NPT ensemble was simulated using velocity rescaling for the temperature coupling and the Parrinello-Rahman barostat for pressure

coupling^{35,36}. Electrostatic interactions were calculated using the particle-mesh Ewald (PME) algorithm³⁷, with a grid spacing of 0.12 and real-space interactions cut off at 1.2nm. Van der Waals interactions were switched at 1.0nm and cut off at 1.2nm.

B. The String Method Algorithm

To determine the minimum free energy transition pathways (MFTP) for the AB \rightleftharpoons CC and AB:TR \rightleftharpoons CC:TR conformations, we used the string method algorithm in collective variables, which was first presented by Maragliano et al⁵. We outline our implementation here; further details can be found in in appendix B and Refs¹⁻⁹.

While a number of powerful methods have been developed to sample transition pathways and other rare events (e.g.,^{6,7,38-54}), the string method provides a means to discover the MFTP in a space of many collective variables (CVs), with a computational expenditure that is nearly independent of the number of CVs. To obtain a meaningful free energy minimum, the collective variables must include all slow degrees of freedom relevant to the transition. Our collective variables were chosen to be a subset of the atomic positions^{6,8,55,56}. Since extraneous collective coordinates can impede sampling within trajectory space, we attempted to find a minimal set of these coordinates sufficient to characterize the transition. To rapidly screen a number of candidate coordinate sets, we performed targeted molecular dynamics (TMD) simulations⁵⁷, in which external biasing forces directing the system between the two stable substates were applied to the candidate atoms. The coordinate sets were then evaluated based on whether they correctly targeted the stable substate, and the drift in RMSD from the target substate after restraints were released.

For a chosen set of coordinates, a string calculation was initialized from the corresponding TMD trajectory. This initial trajectory was then iteratively relaxed toward the MFTP, during which time the sufficiency of the collective coordinates was further evaluated. The free energy profile as a function of arc length along the final converged string was then calculated using umbrella sampling. Details about these procedures, the chosen set of coordinates, and assessments of convergence are given in appendix B.

C. Correlated Motions and mean squared fluctuations (MSF)

The correlated motions between C _{α} atoms in the dimer backbone and the mean squared fluctuations (MSF) for each amino acid about an average structure were calculated for each of the CP₂ and CP₂:TR systems. Each calculation used data from 30 10ns unbiased MD simulations, with coordinates output every ps. The structures were first aligned to minimize the mass-weighted RMSD

of the C_α atoms that comprise the core of the protein (residues 7-63 and 85-124).

Mean squared fluctuations. Using the aligned structures, the MSF was calculated with respect to the average structure and then averaged over all non-hydrogen atoms in each amino acid according to

$$F_i = \langle |\mathbf{r}_i(t) - \bar{\mathbf{r}}_i|^2 \rangle \quad (1)$$

where F_i gives the MSF for atom i with $\mathbf{r}_i(t)$ as the position of atom i at time t , $\bar{\mathbf{r}}_i$ as the average position, and $\langle \dots \rangle$ denotes an average over simulation configurations. The MSF is related to the crystallographic B -factor for each residue R by¹³

$$B_R = \frac{8}{3} \pi^2 \frac{1}{N_R} \sum_{i \in R} F_i. \quad (2)$$

Correlated motions. The correlation of C_α atom displacements from the average structure was calculated according to

$$C_{ij} = \frac{\langle (\mathbf{r}_i(t) - \bar{\mathbf{r}}_i) \cdot (\mathbf{r}_j(t) - \bar{\mathbf{r}}_j) \rangle}{\langle |\mathbf{r}_i(t) - \bar{\mathbf{r}}_i| \rangle \langle |\mathbf{r}_j(t) - \bar{\mathbf{r}}_j| \rangle} \quad (3)$$

where C_{ij} gives the correlation between C_α atoms of amino acids i and j , $\mathbf{r}_i(t)$ is the position of the C_α atom for amino acid i at time t , and $\langle \dots \rangle$ denotes a time average. C_{ij} ranges from -1, for perfectly anti-correlated motion, to 1, for perfectly correlated motion.

We then performed cluster analysis using spectral decomposition on C_{ij} to identify groups of amino acids that tend to have correlated motion with each other. The similarity matrix S_{ij} was constructed, setting anti-correlated amino acids to the minimum ‘‘similarity’’, according to

$$S_{ij} = \text{Max}(C_{ij}, 0). \quad (4)$$

To verify that amino acids within a cluster have significant correlated motion and that amino acids in separate clusters do not, the intra-cluster and inter-cluster averages (respectively) were calculated as:

$$\text{cluster avg} = \frac{1}{N} \sum_{i \in W_m} \sum_{j \in W_n, j \neq i} C_{ij} \quad (5)$$

where W_m is the set of amino acid numbers that belong to cluster m . The sums loop over all residues in W_m and W_n , and N is the total number of elements in the sum such that $i \neq j$. For an intra-cluster average ($m = n$), all amino acid self-correlations are ignored (i.e. $i \neq j$).

D. Mutual Information

We calculated the mutual information (MI) between all pairs of amino acids for all CP₂ and CP₂:TR systems using the approach and MutInf program developed by McClendon et al⁵⁸. In this approach, the MI is calculated using second order terms from the configurational

entropy expansion, and indicates the correlation between side chain conformations⁵⁸. It is calculated using internal coordinates (i.e. the ϕ and ψ backbone dihedrals and side chain rotamers), and thus may be better than Eq. (3) at picking out conformation changes that do not result in a large backbone movement. Amino acids that have shared mutual information have correlated dihedral distributions. Correlated distributions can arise through direct interaction, a chain of interactions, backbone movements, solvent rearrangement, or other mechanisms.

For each system, we applied the MutInf program to 30 10ns trajectories with configurations output every 1 ps. We then used hierarchical clustering on the resulting MI matrix to identify groups of amino acids that share significant mutual information (as done in Ref⁵⁸). We generated the dissimilarity matrix as given in Eq. 6, and used a Euclidean distance metric to cluster amino acids.

$$D_{ij} = \text{Max}(\text{MI}) - \text{MI}_{ij} \quad (6)$$

We systematically extracted the largest possible ‘‘real’’ clusters by recursively splitting the hierarchy of clusters until each cluster achieved an MI average greater than $0.05k_B T$. After generating the clusters, we verified that they were valid (i.e. had high intra-cluster MI averages and small inter-cluster MI averages) using Eq. (5), with MI_{ij} substituted for C_{ij} .

III. RESULTS

A. Conformational Transition Pathway

In this section we compare the calculated most probable conformational transition pathways for the CC \rightleftharpoons AB and CC:TR \rightleftharpoons AB:TR MS2 coat protein dimer interconversions. The free energy profiles calculated from the converged strings and illustrative snapshots from the converged strings are shown in Fig. 2. Details on these calculations can be found in Sections II:A,B and Appendix B. Furthermore, several tests of convergence are discussed in appendix B5. Most significantly, an independent string started from a different initial pathway produced a similar transition pathway and free energy profile (Fig. A4).

1. Pathway in the Absence of TR

The CC \rightleftharpoons AB calculation obtains that the symmetric CC state is favored over the AB state by a free energy of $\approx 3k_B T$, and there is one on-pathway metastable state. The string pathway indicates the following order of events for a CC to AB transition (Fig. 2c): (1) The CC loop bends inward, straining the native backbone hydrogen bonds and eventually breaking them, beginning with the bonds closest to the core of the protein (and Trp82). This process involves a free energy barrier of

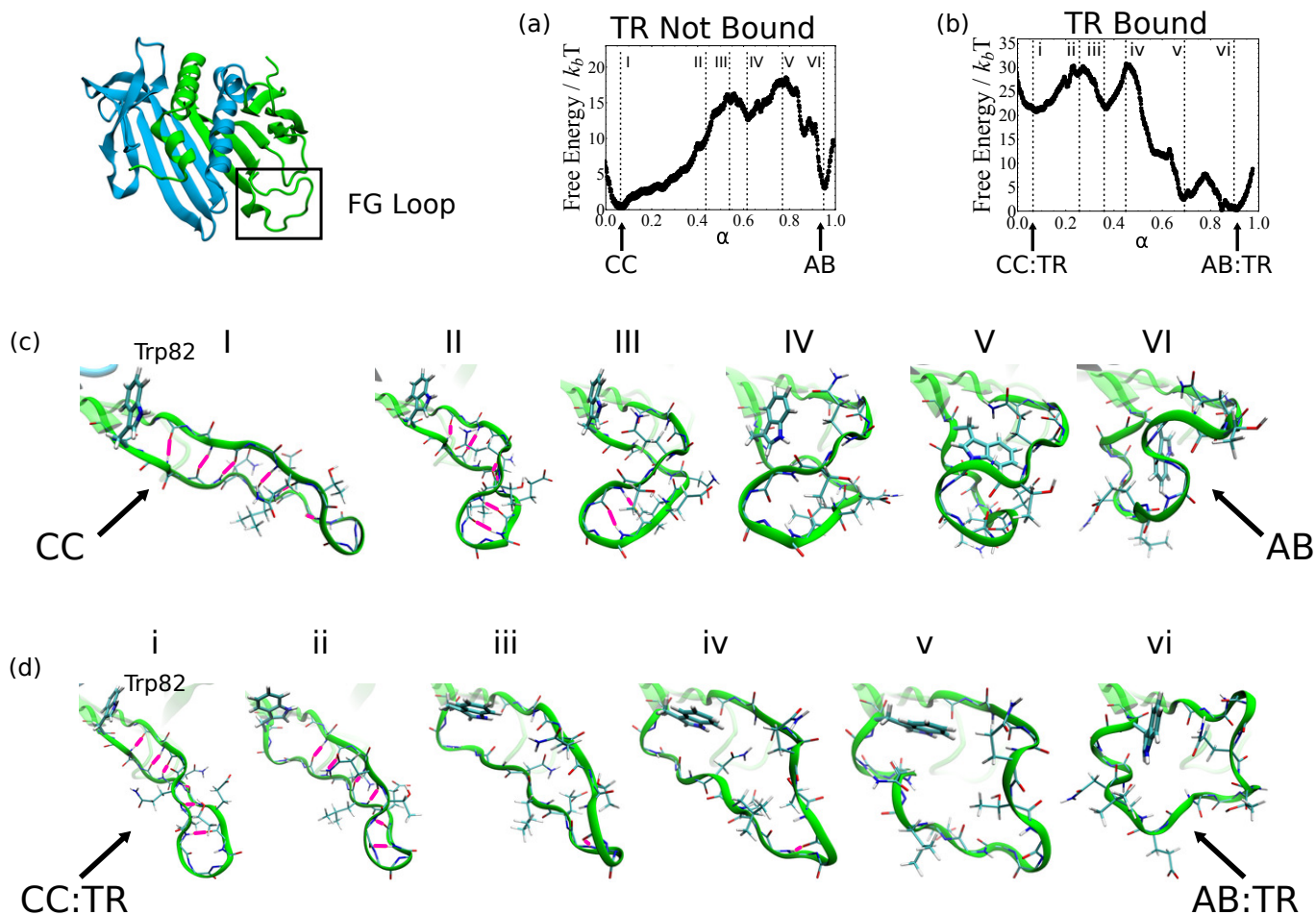


FIG. 2. The most probable transition pathways and associated free energy profiles for $CC \rightleftharpoons AB$ and $CC:TR \rightleftharpoons AB:TR$. (a), (b) The free energy along the most probable pathway as a function of arc length α along the converged strings. (c), (d) Close up snapshots of the B* FG loop along the transition pathway for $CC \rightleftharpoons AB$ (c) and $CC:TR \rightleftharpoons AB:TR$ (d). The native backbone hydrogen bonds of the CC monomer are shown in pink, and side chains with atoms selected as string collective variables (CVs) are shown as bonds. The labels correspond to the position along the free energy profile as indicated in (a) and (b).

about $12k_B T$. (2) After all of the native hydrogen bonds are broken, the FG loop opens and becomes partially solvated. Trp82 now rotates out of the hydrophobic pocket toward the center of the FG loop, leaving the system in a metastable state. (3) The FG loop widens further, surmounting a free energy barrier of $\approx 5k_B T$. (4) The FG loop expansion allows Trp82 to rotate into its final configuration, moving downhill in free energy.

2. Pathway in the Presence of RNA

Complexation of CP_2 with the RNA stem loop TR dramatically shifts the free energy landscape, causing the AB:TR substate to be favored over the CC:TR substate by $\approx 20k_B T$. The transition pathway is also markedly different from $CC \rightleftharpoons AB$, and now involves two on-pathway metastable states (Fig. 2b,d). In the converged string, the transition from CC:TR to AB:TR pro-

ceeds by the following sequence of events: (1) The first two backbone hydrogen bonds near the base of the FG loop break. The backbone dihedral angles of amino acids 79-81 move toward their eventual position in the α -kink of AB:TR. This represents the first barrier to the transition, of $\approx 7k_B T$. (2) It is now free energetically favorable for Trp82 to rotate out of the hydrophobic pocket toward chain A. Interestingly, this rotation proceeds in the opposite direction as found in the $CC \rightleftharpoons AB$ transition. (3) A second barrier of $\approx 7k_B T$ is crossed, involving side chain rearrangements and further solvation of the FG loop. (4) Finally, Trp82 rotates into the FG loop, which then spontaneously collapses, resulting in the second metastable state. This state is structurally very similar to the final AB:TR state, and only $\approx 2k_B T$ higher in free energy. (5) A final rotation of Trp82, involving a $\approx 4k_B T$ barrier, leads to the final AB:TR state.

3. Comparison of Pathways

The most striking difference between the $AB \rightleftharpoons CC$ and $AB:TR \rightleftharpoons CC:TR$ strings is the shift in the most stable sub-state upon TR binding, from CC to AB:TR. This population shift is consistent with experimental data¹². Both pathways highlight the important role of the large side chain of Trp82 in determining the sequence of events during the conformation change. The strings show that the native CC backbone hydrogen bonds require much more substantial molecular rearrangements before breaking and allowing rotation of Trp82 in the $CC \rightleftharpoons AB$ transition as compared to $CC:TR \rightleftharpoons AB:TR$. This difference suggests that the binding of TR destabilizes these hydrogen bonds, which would contribute to shifting the population toward the AB:TR state. To further elucidate the mechanistic differences between the two calculated pathways, we analyzed long unbiased MD simulations of the four stable substates, as described next.

B. Conformation-specific interactions

As shown by the string calculations, the movement of Trp82 defines the key steps during conformation change. In the A and C monomer conformations, Trp82 is pointing back toward the core of the protein with its rotation sterically restricted by Lys66 (of the same monomer) and Phe95 (of the other monomer). We find important differences between the TR-bound and unbound systems along the transition pathway for these and other important interactions. Some of these important interactions were not included as collective variables within the string, but emerged from the string calculation. In this section, we highlight some of these interactions and analyze their behaviors within 300 ns unbiased MD trajectories performed for each of the CC, AB, CC:TR, and AB:TR systems.

1. Phe95 Gate

Phe95 acts a steric gate that can be either “open” or “closed” to the rotation of Trp82 (of the opposite monomer) from its hydrophobic pocket in the A and C conformations (see Fig. 3 d,e). There is one such gate for each of the two monomers: the A* Phe 95 blocks B* Trp82 (we will refer to this as the “B* gate”) and the B* Phe95 blocks A* Trp82 (the “A* gate”). In the converged strings, the B* gate is closed for CP_2 and open for $CP_2:TR$. This difference in steric interactions may explain why the rotation of Trp82 follows different pathways in the TR-bound and unbound strings.

When examining the long, unbiased MD trajectories, we find significant differences between the opening and closing behavior of Phe95 in each of the different systems. The fraction of time each Phe95 gate is open for each system is shown in Fig. 3c. The most striking result is the

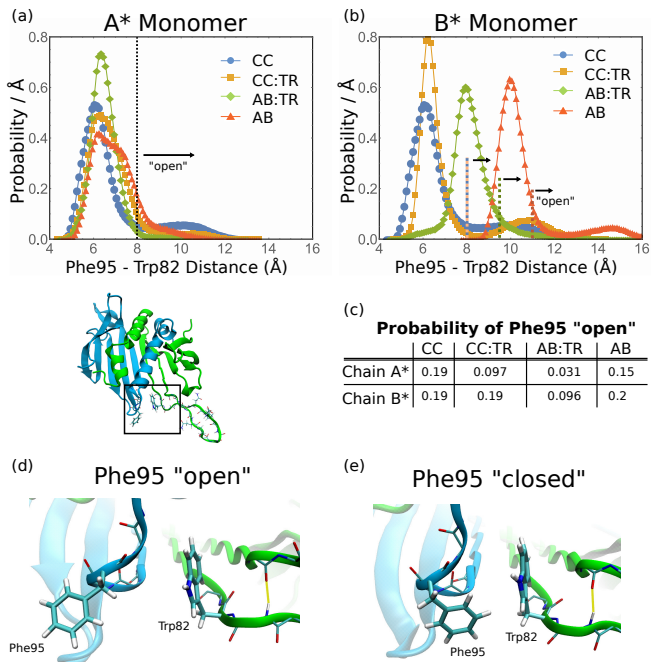


FIG. 3. (a), (b) The probability distribution function for the center of mass distance between Trp82 of monomers A* and B* (respectively) and the neighboring Phe95 (from the opposite monomer). The distance beyond which Phe95 is considered “open”, meaning that Trp82 rotation would not be sterically hindered, is shown on the plot. Note that this distance varies depending on the orientation of Trp82, as shown in (b). (c) The fraction of time that the Trp82 of the indicated chain is able to rotate (the Phe95 gate is open) for each of the four systems. (d), (e) Snapshots of the FG loop showing the Phe95 “open” and “closed” states.

asymmetry that arises between the two monomers after TR binds CP_2 ; TR binding strongly increases the fraction of time that the A* gate is closed (by a factor of 5 in the AB system), whereas the effect on the B* monomer is much weaker. The Phe95 gate opening probabilities (Fig. 3c) do not directly explain the observation that the $CC \rightleftharpoons AB$ string involves a closed gate. However, while opening of the Phe95 gate is transient (the average duration of the open state is ≈ 20 ps), TR binding leads to a 3-fold increase in the probability that the B* Phe95 remains open for 1ns or longer (0.9%). In addition, the Phe95 gate tends to open wider when TR is bound (see Fig. 3 b). These factors should increase the probability of a successful Trp82 rotation in the B* FG loop, and thus favor a conformational transition on B* over A*.

2. Arg83 interactions

Arg83 forms high affinity salt bridges with the backbone oxygen of Ser39 and carboxyl group of Glu66. Although Arg83 is usually tightly bound to both sites in all

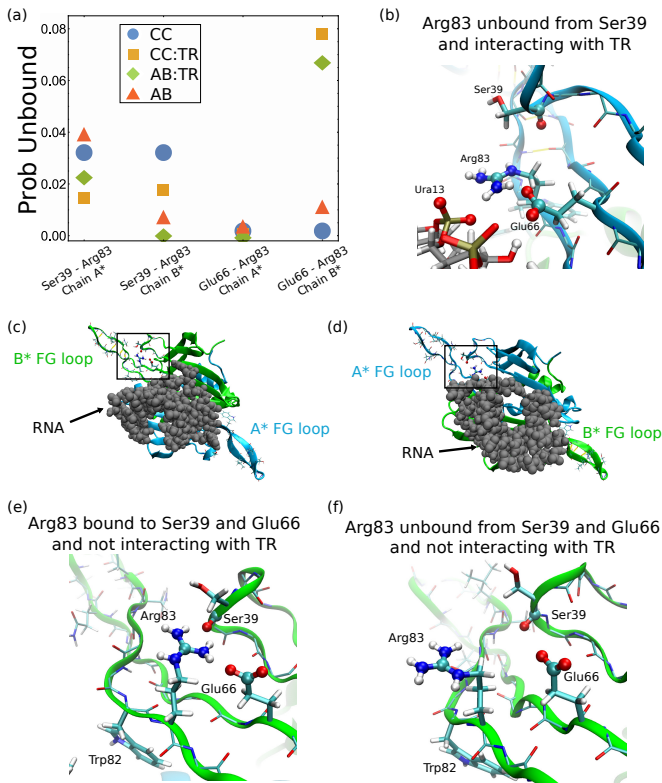


FIG. 4. (a) The probability of Arg83-Ser39 or Arg83-Glu66 interactions in the A* and B* monomers breaking during unbiased MD trajectories. An interaction is considered broken when the favorable interaction energy drops below $4k_B T$ and the COM separation is greater than 6\AA . The interaction energies and COM positions are calculated using the atoms shown as VDW spheres in b,e,f. (c)-(d) Bottom view of the CC:TR dimer. The boxes show the perspective of the snapshots in b,e,f. (b) The A* Arg83-Glu66 bond rarely breaks when TR is bound due to its interactions with the RNA backbone. (e)-(f) Typical interacting and non-interacting states (respectively) when Arg83 and Glu66 are not interacting with TR.

systems, differences are observed between the $CC \rightleftharpoons AB$ and $CC:TR \rightleftharpoons AB:TR$ strings. In the $CC \rightleftharpoons AB$ pathway, both the A* and B* Arg83 residues remain bound to both Ser39 and Glu66 throughout the transition. In the $CC:TR \rightleftharpoons AB:TR$ pathway, the A* Arg83 remains bound, but the B* Arg83 fluctuates away from Ser39 and Glu66 in the B* monomer. Of particular importance, the B* Arg83 unbinds from Ser39 and pulls away from Glu66 immediately before Trp82 first rotates out of its hydrophobic pocket and then again as the α -kink is formed for the AB:TR state.

Fig. 4a shows the probabilities of the Arg83-Ser39 and Arg83-Glu66 salt bridges breaking during the long unbiased trajectories for each system. The most significant result is that TR binding generates an asymmetry between the Arg83-Glu66 salt bridges in the two monomers. For CC:TR and AB:TR, the Arg83-Glu66 salt bridge is eight

times more likely to be broken in the B* monomer than the A*. As shown in Fig. 4b, the decreased likelihood of the Arg83-Glu66 salt bridge breaking in the A* monomer arises in part due to steric restrictions from TR. In addition, both Arg83 and Glu66 of the A* monomer interact strongly with the RNA backbone, which further hinders their separation.

The Arg83-Ser39 salt bridge is conformation dependent, with a higher probability of breaking in A/C monomers than in the B monomer. TR binding causes a general decrease in probability of breaking in both the A* and B* monomers. This interaction may help stabilize the B conformation in the AB:TR state, and could play a role in destabilizing the B* monomer in CC:TR through coupling to increased fluctuations in the neighboring DE loop (discussed in the next section).

C. Mean squared fluctuations

The mean squared fluctuations (MSF) were calculated for each system using 30 10ns unbiased MD simulations as described in Sec. II C. The MSF gives the typical fluctuations for each amino acid and provides insight into the relative flexibility of different portions of the protein (as shown in Fig. 5).

While the CC dimer is symmetric, we find that binding of TR gives rise to asymmetries in the fluctuations of the two monomers. This asymmetry could play a role in shifting the favored conformational state from CC to AB upon binding of TR, as indicated by the string calculations. In particular, in CC:TR, the DE loop fluctuations of the B* monomer are greater than in the A* monomer. The DE turn interacts with the FG loop and shares correlated C_α motion (as described in the next section). Also, the Arg83-Ser39 salt bridge between FG and DE loops (discussed in Sec. IIIB) is more likely to remain intact after TR binds, which coupled with the increased fluctuations of the B* DE loop could destabilize the CC conformation. The binding of TR also causes an asymmetric dampening of fluctuations in the AB loops, with relatively larger fluctuations in the B* monomer. These asymmetries are largely resolved upon a conformation change to AB:TR, with the exception of significantly increased MSF in the A* FG loop and a corresponding decrease in the B* FG loop.

The AB conformation, which is the unfavored state in the absence of TR, also has significant asymmetries in protein dynamics. We find that the MSF of AB loops once again differ between the two monomers, except with larger MSF now found in the A monomer. Although the A FG loop MSF returns to the CC average value, the B FG loop becomes even less flexible. These dynamics may help communicate information across the dimer. Once again, a conformation change to the preferred state (CC) resolves these asymmetries.

Comparison to Previous Results. Dykeman et al¹³ calculated crystallographic B factors (directly re-

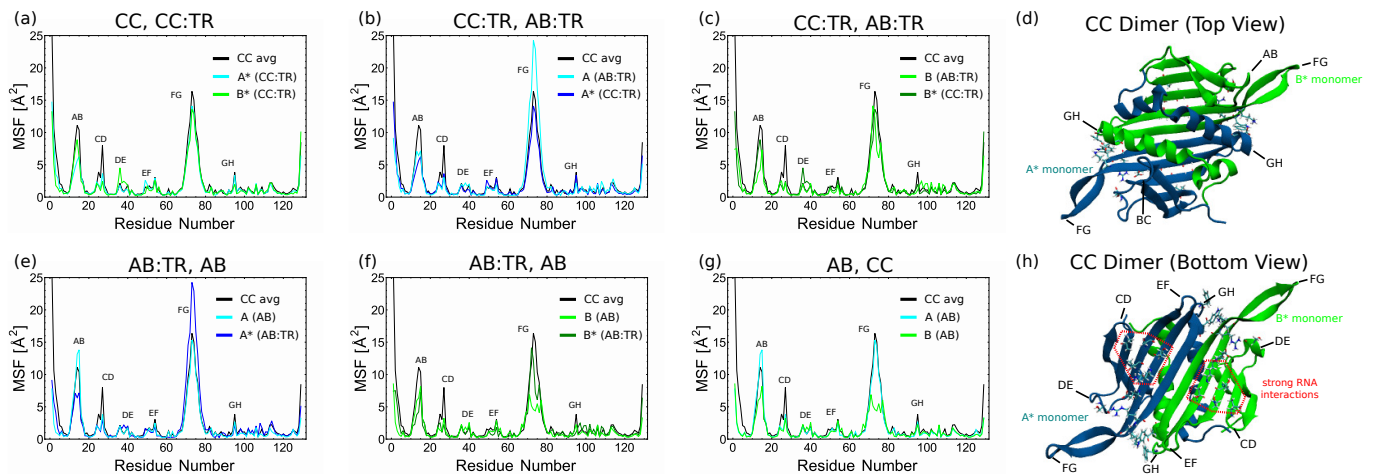


FIG. 5. The MSF for each residue (averaged over all non-hydrogen atoms within a residue) for each system. (a)-(c),(e)-(g) The MSF as a function of residue number with the loops and turns labeled. To facilitate comparison of the dynamics between different systems, each plot shows as a reference the MSF for the CC dimer, averaged over the two symmetric monomers, as well as the two indicated additional systems. (d),(h) The top and bottom view of the CC dimer with the loops and turns labeled according to convention⁵⁹. Important amino acids are also shown as bonds.

lated to MSF through Eq. (2)) using an all-atom normal mode analysis for the CC and CC:TR conformations of WT MS2 and an assembly incompetent mutant W82R. In WT MS2, they find that TR binding causes asymmetries in the fluctuations of the two monomers: the MSF of the EF loop decreases in B* but increases in A*, and the MSF in the FG loop increases in B* but not A*. They find that TR binding to W82R (in a symmetric BB conformation) instead increases fluctuations of the DE loop. It is suggested that this difference in dynamics upon TR binding between the wild type and mutant could play a role in rendering W82R assembly incompetent.

However, in our MSF calculations for the P78N mutant, we find that the asymmetries upon TR binding are confined predominantly to the DE and AB loops, with little difference between the FG and EF loops. Since P78N assembles complete (although non-infectious) capsids, this observation suggests that an asymmetry in DE loop fluctuations does not prohibit assembly. Moreover, our MI calculations (Sec. III E) indicate that allosteric communication does not require an asymmetry in EF loop fluctuations. The differences in MSF calculated here and in Ref.¹³ may be due to sequence difference (WT vs P78N) or the different approaches and force fields: normal modes with the AMBER force field and implicit solvent¹³ compared to MD with the CHARMM force field and explicit water (this work).

D. Correlated Motion

To characterize how TR binding affects dynamics across the protein, we calculated single-time pair correlations in displacements of C_{α} positions for all residue

pairs in each CP₂ and CP₂:TR system (Sec. II C). To find groups of amino acids that tend to exhibit correlated movement, spectral decomposition was used to cluster C_{α} atoms based on the correlation matrix. These clusters are presented in Fig. 6, and their validation is discussed in Appendix C.

In all the CP₂ and CP₂:TR systems, we find a cross-dimer correlation between CD loops due to a common normal mode. We also see a cross-dimer correlation between the FG loops in CC and CC:TR, with intra-cluster correlation averages of around 0.2. Since this cross-dimer correlation is not present in the AB and AB:TR systems, this observation suggests that mechanical communication between FG loops along the backbone is conformation-specific.

As in the MSF calculations, we find an asymmetry between AB loops in both non-preferred states, CC:TR and AB. In CC:TR, we find that the AB loop of the B* monomer experiences greater fluctuations than the A* AB loop, but no longer shares correlated motion with any other portion of the dimer (unlike the A* AB loop). In AB, we again find that the AB loop of the B monomer has no cross dimer correlations; however, the AB loop of the A monomer has correlated motion across the dimer with the FG loop of the B monomer. Of particular significance, this AB loop undergoes significantly increased fluctuations in the AB state (Fig. 5g), which are mechanically communicated across the dimer to the site of the conformation change.

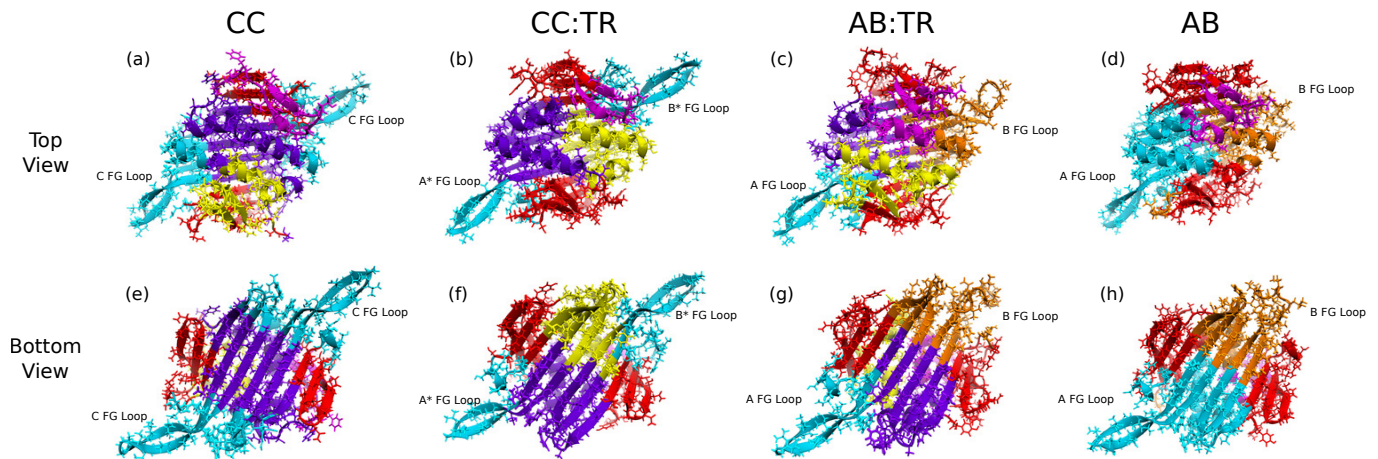


FIG. 6. Clusters of amino acids whose C_{α} atoms have correlated motion in each CP_2 and $CP_2:TR$ system. (a) - (d) The top view of the dimer and (e) - (h) the bottom view of the dimer. Distinct clusters are distinguished by color. TR is rendered invisible for CC:TR and AB:TR to aid visibility.

E. Mutual Information

To characterize residue conformational correlations, we calculated the mutual information between the dihedral angles of all pairs of amino acids. The calculation was performed for each system using long unbiased simulations as described in Sec. IID. Amino acids that share mutual information with each other were then grouped using hierarchical clustering⁵⁸ and an iterative process that extracted the largest possible clusters with an intra-cluster average of at least $0.05k_B T$. The results from this clustering calculation are shown in Fig. 7. To verify that these clusters were distinct from each other (i.e. amino acids in different clusters share little mutual information), we calculated all inter-cluster averages (Appendix D).

The MI results indicate that correlations are spread across the bottom of the dimer in the AB:TR and CC:TR states, as illustrated by the large clusters in Figs. 7f,g, whereas correlations are more localized in the AB and CC states, as illustrated by the smaller more fragmented clusters in Figs. 7e,h. When TR binds to CP_2 , there is a binding pocket in each monomer comprising the same five amino acids (Val29, Thr45, Ser47, Thr59, Lys61), which strongly interacts with the Ade nucleotides at positions -4 and -10 respectively⁶⁰ (see Fig. 1f for the numbering scheme). The conformations of these five residues are therefore directly and strongly influenced by TR binding; so to investigate the effect of TR binding across the protein we looked for other residues correlated to these five binding pocket residues. The binding pocket residues form parts of large clusters in CC:TR and AB:TR (predominantly the off-green and light pink colored clusters in Fig. 7f,g), indicating that effects of TR binding are broadly communicated. Of particular interest, the binding pocket residue Thr45 is found in the same cluster

as Trp82, Arg83, Glu66, and Ser39 in the B^* monomer of two non-preferred states (CC:TR and AB). Recalling the pivotal roles identified for these residues in the dimer conformation change (see sections III A and III B), these correlations may reflect part of the mechanism by which TR influences the preferred conformational state.

MI clusters which extend over large distances are of particular interest, since perturbations to an amino acid within such a cluster can generate a response from distant residues within the same cluster. One such cluster is found in the (non-preferred) CC:TR state with amino acids spanning between the A^* FG turn and the B^* AB loop (the pink cluster in Fig. 7 b). As shown in Secs. III C and III D, the B^* AB loop does not have correlated motion with the rest of the dimer, but does experience larger fluctuations than the A^* side. After undergoing a conformation change to AB:TR, this cluster now instead encompasses the FG loops of both monomers (the pink cluster in Fig. 7 c) and thus could provide a mechanism for conformational selection.

Another interesting MI cluster appears in the AB substate (the green cluster in Fig. 7 h). This cluster contains the B FG loop and distant residues across the dimer, including Arg83 and Glu66 (of the A monomer). The conformations of these residues are altered upon TR binding (Sec. III B 2). This cluster also has a small amount of shared information with the A^* AB loop, which has significantly increased fluctuations compared to the B^* monomer and correlated motion with the FG loop (as shown in Secs. III C and III D). Since this cluster contains amino acids that have dynamics altered by TR unbinding, these correlations may also reflect part of the conformational selection mechanism.

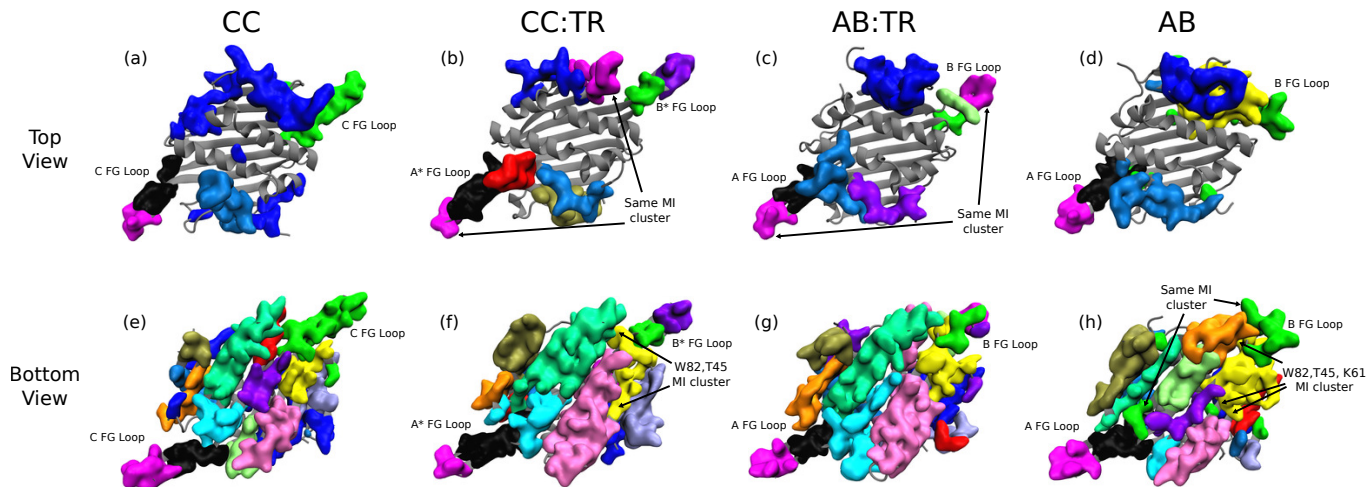


FIG. 7. Mutual information clusters for the AB, CC, AB:TR, and CC:TR systems. The clusters of correlated residues, calculated from the mutual information between pairs of amino acids as described in the text, are shown in different colors on a gray protein backbone with the same orientation as in Fig. 5 d,h. (a) - (d) Top view of the dimer, with selected clusters of correlated residues in the FG and AB loops. (e) - (h) Bottom view of the dimer with all clusters shown and clusters that span large distances labeled. The yellow cluster in CC:TR (f) and AB (g) contains Trp82 of B* (along with Arg83, Glu66, and Ser39) and at least one amino acid that strongly interacts with TR. This is not the case for A* or either monomer in the two populated substates (CC (e) and AB:TR (g)).

IV. DISCUSSION AND CONCLUSIONS

We have combined the string method, free energy calculations, and analysis of long unbiased molecular dynamics simulations to characterize the effect of binding of the MS2 genome fragment TR to its capsid protein. The calculations demonstrate that the impact of TR binding is substantial and far-reaching. The free energy profiles calculated from our converged strings for the $CC \rightleftharpoons AB$ and $CC:TR \rightleftharpoons AB:TR$ transitions (Fig. 2) show a strong shift in the favored population from CC to AB:TR. Furthermore, the strings indicate that TR binding dramatically alters the interconversion pathway, changing the sequence of events and the nature and number of intermediate metastable states. Given that TR binds more than a nanometer from the residues which undergo the majority of conformational rearrangement (the FG loop), our calculations provide direct evidence for allostery and begin to reveal its underlying mechanisms, albeit within the limitations of force field accuracy and finite sampling.

The fundamental effect of TR-binding is to generate an inherently asymmetric dimer. The $CC \rightarrow AB$ transition requires a spontaneous fluctuation that breaks the CC symmetry and ‘chooses’ which FG loop will interconvert to a B conformation. In contrast, TR-binding introduces subunit-spanning asymmetries that favor transition of one chain. We characterized these asymmetries, and how they are transmitted across the protein, by analyzing collective motions and correlated conformational statistics of amino acids within long unbiased MD trajectories of each stable substate. We found extensive asymmetries in both the dynamics and conformational statis-

tics; we particularly focused on asymmetries which are reflected in different molecular-scale interactions within the $CC \rightleftharpoons AB$ and $CC:TR \rightleftharpoons AB:TR$ converged strings.

We identified several such interactions. Most notably, Phe95 acts a steric gate, which when “closed” impedes the rotation of Trp82 required for a transition between C to B monomer conformations. TR binding significantly increases the probability of the A* Phe95 gate being closed, while tending to increase the width of the open B* Phe95 gate, thus strongly biasing which chain will interconvert. Similarly, Arg83 forms high affinity salt bridges with Ser39 and Glu66. In the unbiased MD simulations, TR binding leads to an eight-fold increase in the probability of the B* Arg83-Glu66 salt bridge breaking. Consistent with this observation, the B* Arg83 salt bridges break during the $CC:TR \rightleftharpoons AB:TR$ string pathway but remain intact during the $CC \rightleftharpoons AB$ string. Since in the CC:TR substate, Ser39 and Glu66 are present in clusters of residues with correlated conformational statistics that include residues which directly bind to TR, the salt bridges provide a mechanism by which TR binding communicates with the FG loop. We also speculate that these salt bridges may preferentially stabilize the B FG loop conformation.

Comparison to previous results. Previous experiments on MS2 have shown that TR binding induces a conformational change from a symmetric to an asymmetric structure¹². Based in this and other evidence it has been inferred that the CC state is preferred in the absence of TR, and the AB state in the presence of TR. Our results from the string method calculation and the associated free energy profile directly support this conclusion, and

also reveal that the associated transition pathways differ in the presence of TR.

A study by Dykeman et al¹³ performed an all-atom normal mode analysis to determine how the vibrational modes are modified by RNA binding. They found that TR binding to a (WT) CC conformation causes asymmetric fluctuations of the EF loop; fluctuations increase in A* and decrease in B*. The mutant W82R has an asymmetry in the DE loop instead, which was proposed as a possible explanation for why it is assembly-incompetent. In contrast, our MSF calculations find that asymmetries upon TR binding are confined predominantly to the DE and AB loops, with little difference between the FG and EF loops fluctuations. This suggests that an asymmetry in EF loop fluctuations is not required for capsid assembly, and that an asymmetry in DE loop fluctuations does not necessarily hinder assembly. The differences in MSF calculated here and in Ref.¹³ may be due to differences in sequence (WT vs P78N), computational approaches, force fields, or implicit versus explicit solvent.

Limitations of our calculations and outlook. Recent computational studies have shown that conformational transitions can proceed by multiple, diverse pathways (*e.g.*⁶¹), while a single string calculation typically samples only one transition tube. However, in our system, independent string calculations started from substantially different initial pathways led to very similar converged strings (Fig. A4), consistent with efficient sampling in trajectory space. While we analyzed correlations of amino acid conformations within the stable conformational substates, further insight into the transition mechanism might be obtained by characterizing mutual information during the conformational transition. Finally, in this work, we focused on the effects of TR binding on the coat protein dimer conformations. A natural next step is to examine the effect of TR binding on dimer-dimer interactions; *e.g.* Ref.¹⁴.

ACKNOWLEDGMENTS

This work was supported by Award Number R01GM108021 from the National Institute Of General Medical Sciences. Computational resources were provided by the NSF through XSEDE computing resources (Trestles, Kraken, and Queen Bee) and the Brandeis HPCC which is partially supported by the Brandeis Center for Bioinspired Soft Materials, an NSF MRSEC, DMR-1420382.

Appendix A: Additional methods details

1. Equilibration

Each of the 4 systems was relaxed from its initial configuration as follows. First, the system was minimized

while iteratively relaxing harmonic restraints on all protein heavy atoms, centered on crystal structure positions. Next, MD simulations were performed in which the same restraints, now centered on the final minimized position, were slowly relaxed as the temperature was gradually increased from 25K to 300K. Unbiased MD was then performed for 50-100ns to ensure equilibration. To prevent self-interaction, rotational drift was limited by harmonic restraints on the α -carbons of residues 105-109 in the A subunit α -helix, which is located on the top of the dimer far from the FG-loop and RNA binding sites.

Of the four systems, only the AB dimer undergoes significant rearrangement. Trp82 in the FG loop rotated and the rest of the FG loop moved toward the EF hairpin of the A monomer; in contrast, the AB:TR FG loop remained close to the DE loop of the B monomer. The difference between equilibrated AB and AB:TR states is significant because Trp82 is a large side chain which rearranges substantially during the conformational changes.

Appendix B: String method calculations

This section presents details on the string method calculation. Following Ovchinnikov et al.⁶, we define N_{cv} collective variables that depend on the Cartesian positions \mathbf{x} of atoms in the protein as $\boldsymbol{\theta}(\mathbf{x}) = (\hat{\theta}_1(\mathbf{x}), \hat{\theta}_2(\mathbf{x}), \dots, \hat{\theta}_{N_{cv}}(\mathbf{x}))$. Each image n of the string evolves according to⁶

$$\boldsymbol{\theta}_n(t + \Delta t) = \boldsymbol{\theta}_n(t) - \gamma^{-1} \Delta t \mathbf{M}(\boldsymbol{\theta}_n(t)) \nabla G(\boldsymbol{\theta}_n(t)) \quad (\text{B1})$$

where $\boldsymbol{\theta}_n(t)$ gives the collective variable values of image n from string iteration t and γ is a tuneable ‘‘friction constant’’ that sets the size of the step taken down the free energy gradient (along with Δt). The metric tensor $\mathbf{M}(\boldsymbol{\theta}(t))$ accounts for the curvilinear nature of the collective variables and is given by⁶

$$M_{ij}(\boldsymbol{\theta}) = \sum_k \frac{1}{m_k} \left\langle \frac{\partial \hat{\theta}_i(\mathbf{x})}{\partial x_k} \frac{\partial \hat{\theta}_j(\mathbf{x})}{\partial x_k} \right\rangle_{\hat{\boldsymbol{\theta}}(\mathbf{x})=\boldsymbol{\theta}} \quad (\text{B2})$$

where the sum ranges over each coordinate k for all atoms in the system, $\langle \dots \rangle$ denotes an average over sampling constrained in the vicinity of $\boldsymbol{\theta}$, and m_k is the mass of atom k .

We made two simplifying approximations in our implementation. Since we used only Cartesian coordinates for collective variables, we approximated the tensor $M(\boldsymbol{\theta}_n(t))$ in Eq. (B1) as the identity matrix. Tests with and without this approximation supported that the metric tensor can be neglected for our system. The second approximation was to dynamically set $\gamma^{-1} \Delta t$ (from Eq. (B1)) such that the step size is a fixed fraction of the image spacing. This guarantees that new images will not jump too far in any given iteration. With the alanine dipeptide model system, we extensively tested our implementation with both approximations against a string

implementation with collective variables based on dihedral angles.

To identify collective variables sufficient to describe the transition between states, we systematically vetted candidate coordinates using restrained targeted molecular dynamics simulations⁶ (described for our systems in Appendix B1). Next, we used TMD to generate an initial string connecting the two metastable states. This pathway was then discretized into images, and the string was systematically relaxed by the following iterative procedure.

1. **Sample.** For each image n , run short simulations to estimate $\nabla G(\boldsymbol{\theta}_n)$ (the free energy gradient in collective variable space in the proximity of image n). In each short simulation, impose a harmonic potential for each collective variable, centered on the image. The spring constant of the harmonic potential is selected to keep sampling in the vicinity of its image (typically with an average sampling radius of 1-2 image spacings). Calculate the average force imposed by each potential.
2. **Evolve.** Generate a new string by displacing each image a distance δ in the direction opposite to the free energy gradient. In our implementation, δ is scaled to be a fixed fraction of the image spacing.
3. **Reparameterize.** Redefine the locations of images along the string so that they are uniformly spaced in arc length.

This procedure was iterated until the string pathway approximately converged, which was assessed by the RMSD between the initial and current strings. We define the RMSD between strings as

$$\text{RMSD}(\boldsymbol{\theta}^{\mathcal{S}_1}, \boldsymbol{\theta}^{\mathcal{S}_2}) = \left(\int_0^1 |\boldsymbol{\theta}^{\mathcal{S}_1}(\alpha) - \boldsymbol{\theta}^{\mathcal{S}_2}(\alpha)|^2 d\alpha \right)^{1/2} \quad (\text{B3})$$

with $\boldsymbol{\theta}^{\mathcal{S}_i}(\alpha)$ as the N_{cv} -dimensional point at fraction α along string \mathcal{S}_i . Since the strings are discretized, it is necessary to interpolate between images.

1. Selecting Collective Variables

A string is defined by a set of collective variables (CVs), which must include all slow degrees of freedom that are relevant to the reaction. It is not known *a priori* which CVs constitute a good reaction coordinate. While in principle it is possible to choose a large number of CVs with the expectation that a subset of them will constitute a good reaction coordinate, extraneous or redundant CVs can introduce noise that slows convergence. Thus, our goal was to select the minimal possible CV set sufficient to describe both the CP₂ and CP₂:TR conformational transitions.

Based on extensive trial calculations using various types of CVs (including distances, positions, and dihedral angles), we found Cartesian positions of individual atoms to be best suited for the study of MS2. Atomic positions have been successfully used in previous studies^{6,8,55,56} and can capture both the native CC backbone hydrogen bonds breaking/forming and the formation of the α -kink in the AB state.

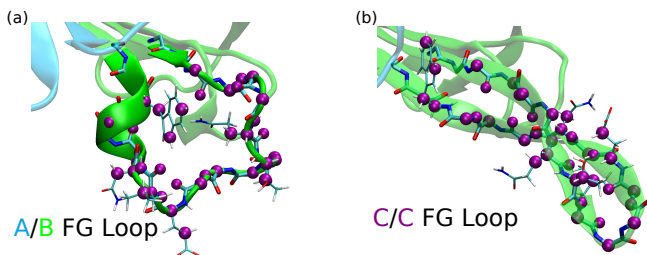
Because absolute positions are not invariant under rigid body motions, we restricted translational and rotational diffusion by including position restraints on 10 C _{α} atoms in the top helices of each monomer in CP₂ (residues 105-109). These residues are far from the RNA binding site and FG loop (where the conformational change is localized). In an alternate approach, Ovchinnikov et al. performed principle component analysis on the rigid core of the protein to define a body-centered coordinate system⁶. Another approach is to perform on the fly structural alignment⁶².

To select the set of atoms whose positions comprise the CVs, we ran a series of targeted molecular dynamics simulations (TMDs)⁵⁷, in which external biasing forces were applied to the candidate atoms to force the system between conformations. Each candidate set of atoms was ranked by the difference in backbone dihedral angles between the final structure and the target, and the amount of RMSD drift observed during 4ns of simulation after all restraints were released. This test was performed on TMD simulations in both directions (AB to CC and CC to AB) for both CP₂ and CP₂:TR. Once a set of CVs was chosen in this manner, redundant or extraneous atoms were eliminated through a trial and error process in which candidate removals were tested by additional TMD simulations. The final set of CVs contains the positions for 40 atoms, listed in Fig A1.

TMD parameters. TMD simulations imposed a harmonic potential as a function of the RMSD difference between the current and target structure, measured from the positions of the candidate CV atoms only. The center of the potential was moved linearly from the RMSD of the initial configuration to 0 over 1.5 ns. The spring constant was linearly scaled from $k = 2.5 \times 10^6 \text{kJ/mol} \cdot \text{nm}^2$ to $k = 5 \times 10^6 \text{kJ/mol} \cdot \text{nm}^2$ over this same interval. After centering on RMSD=0, k was linearly increased over three separate 500ps intervals to $k = (2, 20, 200) \times 10^7 \text{kJ/mol} \cdot \text{nm}^2$. After this, k was linearly decreased to 0 over 1ns, followed by 4ns of unbiased simulation.

2. Generating the Initial String

Initial strings were generated from TMD trajectories of the CC→AB and CC:TR→AB:TR transitions, with the TMD bias based only on CV atoms. Coordinates were saved every 2ps and used to construct a time series of CV values, which was then smoothed to prevent noise from dominating image selection. The data was



String CV List: K66:CA, K66:O, V67:CA, A68:N, A68:CA, A68:O, T69:CA, Q70:N, Q70:CA, Q70:CB, Q70:O, T71:CA, T71:CB, V72:N, V72:CA, V72:O, G73:CA, G74:CA, V75:N, V75:CA, V75:O, E76:CA, E76:CG, L77:N, L77:CA, L77:CG, L77:O, N78:N, N78:CA, N78:CB, V79:N, V79:CA, V79:O, A80:CA, A81:N, A81:CA, W82:CA, W82:CB, W82:NE1, W82:CH2

Orientation Restraint Atoms (on both chains): V105:CA, K106:CA, A107:CA, M108:CA, Q109:CA

FIG. A1. The atoms whose positions were selected as CVs for the string are shown for both the AB and CC FG loops. The backbone and a selection of the side chains are shown as bonds, and the string atoms are shown as purple spheres. The string atoms are listed in the text below the figure along with those atoms whose positions were used to prevent translational and rotational diffusion.

smoothed by applying a nearest neighbor smoothing kernel to the coordinates for 10-20 iterations. Forty images, with approximately equal spacing, were then selected from the smoothed trajectory and used as the initial string pathway. The spacing between the N_{cv} -dimensional images in the initial string was 3.5Å for CP₂ and 2.5Å for CP₂:TR, which provided sufficient resolution to capture bond-breaking and all significant conformational rearrangements.

3. Running the String

Each string was evolved according to the three steps outlined at the beginning of Appendix B: sample, evolve, reparameterize. In the sample step, for each image n , the structure from the previous (or initial) string closest in CV space to the image CV values θ_n was subjected to a steered molecular dynamics (SMD) simulation targeting θ_n . A harmonic potential with force constant $k_{drag} = 100000.0\text{kJ/nm}^2$ was imposed for each CV, and moved linearly to θ_n (at a speed of no faster than 0.1nm/(1000steps)). Then, we sampled the local free energy gradient by performing MD for an additional 200ps with harmonic restraints for the CV centered at θ_n . To maintain local sampling while speeding convergence, we chose a restraint force constant of $k_{hold} = 450.0\text{kJ/nm}^2$, yielding an average sampling radius of 1-2 image spacings. CV values were recorded every 0.1ps. The string was then evolved by updating CV values according to Eq. B1, with a step size set to a fixed fraction $\delta = 0.5$ of the image spacing, followed by reparameterization to maintain uniform spacing along the arc length.

To monitor string convergence, we calculated the

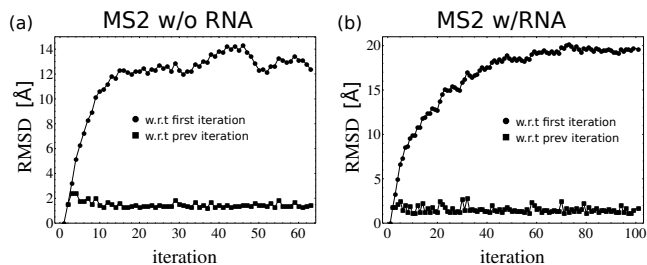


FIG. A2. The RMSD during the equilibration of the (a) CP₂ and (b) CP₂:TR strings. The RMSD is calculated according to Eq. (B3) with respect to both the initial string and the previous string iteration.

RMSD (in CV space) between points at equal arc length along the string according to Eq. B3. We used a linear interpolation between neighboring images to calculate the RMSD at arc lengths not commensurate with image locations. Each string was run until the RMSD with respect to the initial string plateaued, which required 50-100 iterations (Fig. A2).

4. Free Energy Along String Pathway

To calculate the free energy profiles from converged strings, we performed umbrella sampling on an order parameter s that gives the position along the string path. Our implementation is based on the approach described in Ref⁶¹. To ensure that sampling does not meander arbitrarily far in directions transverse to the transition tube defined by the string⁸, we also defined an order parameter z , which measures the distance from the string. The definition of s and z are inspired by the path collective variables in PLUMED²⁹; for an arc length between images i and $i + 1$, s and z are given by

$$s = i + \frac{(\mathbf{y} - \theta_i) \cdot (\theta_{i+1} - \theta_i)}{|\theta_{i+1} - \theta_i|^2}$$

$$z^2 = \frac{|\mathbf{y} - \theta_i|^2}{|\theta_{i+1} - \theta_i|^2} - (s - i)^2 \quad (\text{B4})$$

where θ_i gives the vector of CV coordinates defined by image i , \mathbf{y} is the dynamic vector of CV coordinates during sampling, and s is the projection of \mathbf{y} onto the line segment between the bounding images $(\theta_{i+1} - \theta_i)$, scaled by the image separation.

During umbrella sampling approximately 150 window centers were spaced evenly in s , with a spring constant of $\kappa \approx 350\text{kJ}$. To maintain sampling near the center of the transition tube⁸, a half-harmonic, upper wall potential was placed between $z = 2$ and $z = 3$, with spring constant $\kappa_{wall} \approx 450\text{kJ}$.

To check for hysteresis, each window was seeded using steered MD simulations from two different starting structures, one from each of the upper and lower bounding images. The two seeds for each of the ≈ 150 windows

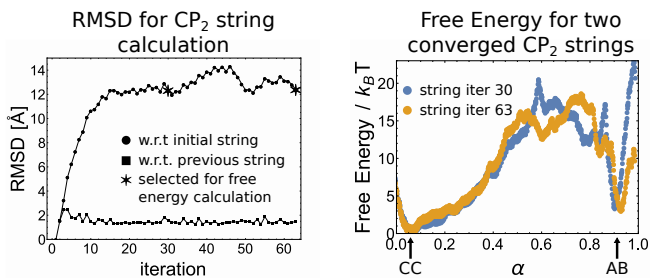


FIG. A3. (a) The string RMSD as calculated from Eq. (B3) during the convergence of a CP₂ string. The strings at iterations 30 and 63 were taken for the free energy calculation (as marked by the stars). (b) The free energy profile for each of the two converged CP₂ strings as a function of arc length α .

were then each sampled for 200ps, so the total simulation time for each free energy calculation was 60 ns. The free energy was calculated from this data using Alan Grossfield’s implementation of WHAM (Weighted Histogram Analysis Method)⁶³.

5. String Convergence and Validity

To test the assumption that a plateau of the RMSD in CV space is a good measure of string convergence, we calculated the CC \rightleftharpoons AB free energy profile for two string iterations after the RMSD plateau (Fig. A3). Although the two free energy profiles are not identical, they obtain the same free energy difference between CC and AB substates, nearly the same barrier height, and both have a single on-pathway metastable state.

To assess global convergence of the string, we performed a second string calculation for the CC:TR \rightleftharpoons AB:TR transition, initialized from a different TMD simulation. This TMD used a slightly different definition for the CC:TR and AB:TR substates, and produced an initial pathway which differs substantially from the initial pathway used for the first string. The RMSD of 13Å between the two initial pathways is approximately as large as the RMSD between the first converged string and its initial pathway. The convergence and resulting free energy profiles are shown in Fig. A4. Once again, the two strings result in the same relative free energies for the CC:TR and AB:TR substates and contain the same number (two) of on-pathway metastable states. While there are quantitative differences, the overall similarity between the two calculations suggests that the strings have converged to the same pathway. This result from two different initial pathways is consistent with a global MFTP, although a thorough assessment would require a number of additional strings and hence a large computational cost.

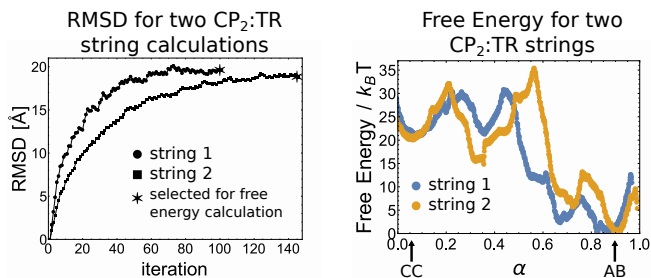


FIG. A4. (a) The RMSD with respect to the initial string (Eq. B3) during the convergence of CP₂:TR strings initialized from two independent TMDs. (b) The free energy profiles for the two final CP₂:TR strings as a function of arc length α .

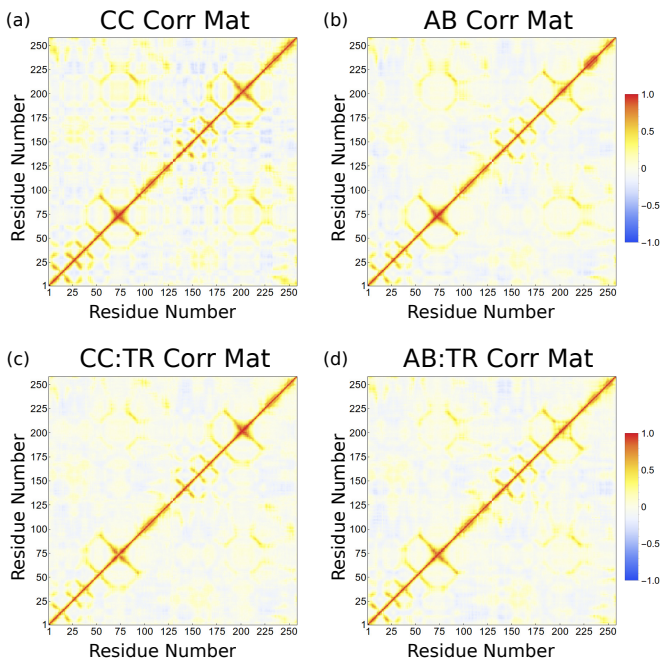


FIG. A5. The correlation matrices for each system. The scaling is shown in the right and is the same for all plots. The amino acids are numbered from 1 to 129 for the A* monomer and 130 to 258 for the B* monomer.

Appendix C: Correlated Motion Calculations

The correlation of vector displacements from the average structure was calculated between the C_α atoms for each amino acid according to Eq. (3). Each structure was first aligned to the average structure to minimize the weighted RMSD of the C_α atom positions that comprise the core of the protein (residues 7-63 and 85-124). The calculation was performed for each system, using 30 10ns unbiased simulations with coordinates output every 1ps. The resulting correlation matrices for each system are presented in Fig. A5. The anti-parallel β sheets are clearly visible as lines with a slope of -1.

We applied spectral clustering to the correlation matrix

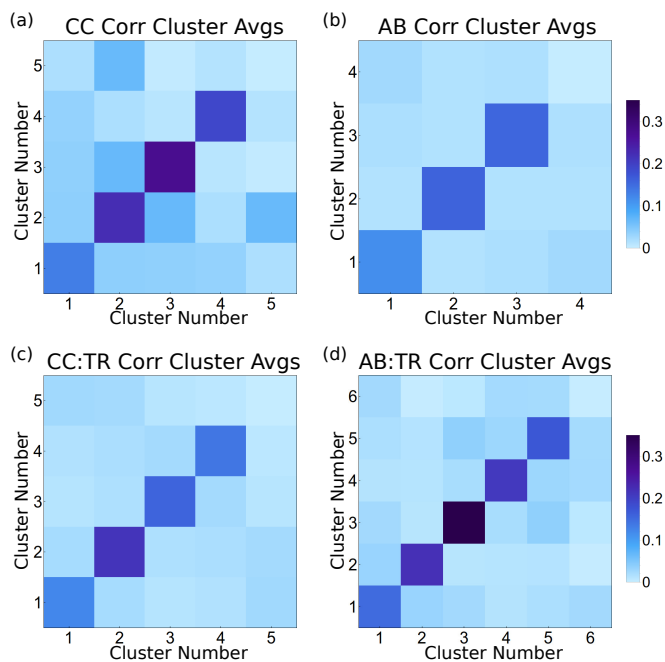


FIG. A6. The similarity matrix for the correlated motion clusters for each CP_2 and $CP_2:TR$ system. The coloring indicates the average correlation and is scaled uniformly for all plots (as shown on the right). The last cluster in each plot contains amino acids that do not share correlated motion with each other or other clusters, which is why the last diagonal element has a value near 0. This corresponds to the magenta colored group in each CP_2 and $CP_2:TR$ system shown in Fig. 6.

ces to identify groups of amino acids that exhibit collective motions. In this method, the spectrum of eigenvalues from a “similarity” matrix are used to reduce the problem’s dimensionality before clustering using k -means⁶⁴. In this case, the similarity matrix is defined by the correlation between any two amino acids, with negative correlations set to 0 (Eq. (4)). The resulting clusters are presented in Fig. 6. We applied Eq. 5 to check that these clusters reflect actual correlations, meaning that intra-cluster correlations are high and inter-cluster correlations are low. The results are shown in Fig. A6, where the diagonal shows strong intra-cluster correlations.

Appendix D: Mutual Information Calculations

The mutual information (MI) between all pairs of amino acids was calculated for each system using the approach and MutInf program developed by McClendon et al⁵⁸, using both backbone and side chain dihedral angles. For each system, we applied the MutInf program to 30 10ns unbiased trajectories, with configurations saved every 1ps. The raw MI matrices are presented in Fig. A7, with a log color scale to accentuate the differences. The anti-parallel β sheets are clearly visible as lines with a

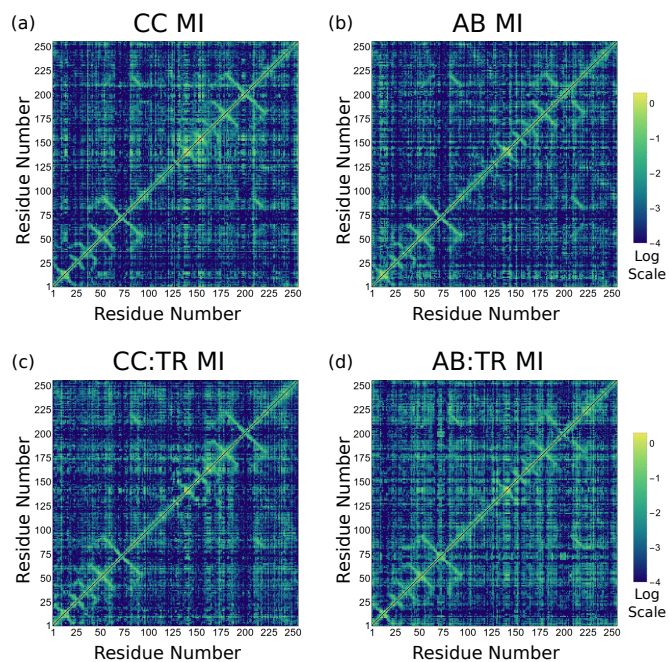


FIG. A7. The mutual information matrices for each system, with coloring shown on a log scale on the right in units of $k_B T$ (ranging between 10^{-4} and $\log_{10} 2$). The amino acids are numbered from 1 to 128 for the A^* monomer and 129 to 255 for the B^* monomer (the mutual information for residue 129 of A^* and residues 1, 129 of B^* was not calculated by MutInf).

slope of -1.

To determine groups of amino acids that have correlated distributions, we then used hierarchical clustering on the MI matrices. In hierarchical clustering, each amino acid starts in its own cluster, and clusters with minimal “dissimilarity” are recursively merged until only one cluster remains. For our calculation, the “dissimilarity” was determined by the intra-cluster average of D_{ij} of Eq. (6). From the resulting hierarchy of clusters, we systematically extracted the largest possible clusters, such that the intra-cluster MI average was greater than $0.05k_B T$. These were presented in Fig. 7 and tested to ensure that they have a high intra-cluster correlation average and a low inter-cluster correlation average (as calculated from Eq. 5). The resulting correlations are shown in Fig. A8, where the diagonal shows strong intra-cluster correlations.

¹E. Weinan, W. Ren, and E. Vanden-Eijnden, Phys. Rev. B **66** (2002).

²W. E, W. Ren, and E. Vanden-Eijnden, J. Chem. Phys. **126** (2007).

³W. E and E. Vanden-Eijnden, Annu. Rev. Phys. Chem. **61**, 391 (2010).

⁴E. Weinan, W. Ren, and E. Vanden-Eijnden, Chem. Phys. Lett. **413**, 242 (2005).

⁵L. Maragliano, A. Fischer, E. Vanden-Eijnden, and G. Ciccotti, J. Chem. Phys. **125** (2006).

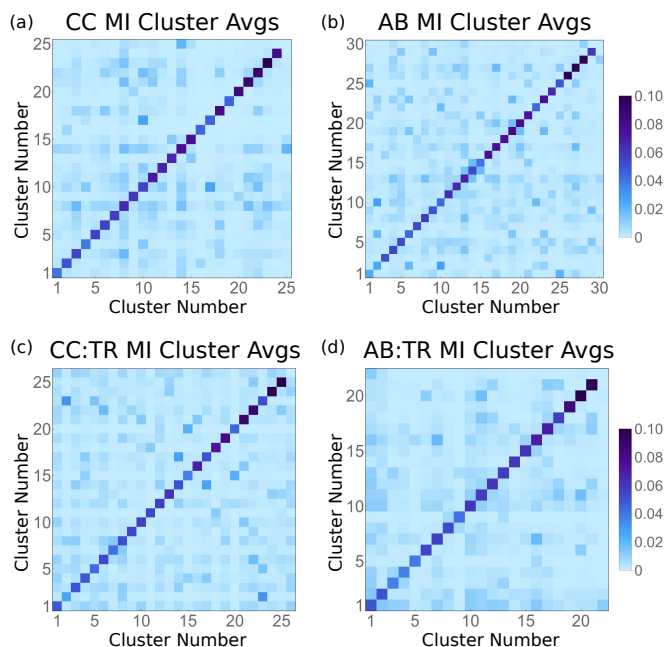


FIG. A8. The similarity matrix for the mutual information matrix clusters for each CP_2 and CP_2 :TR system. The coloring indicates the average mutual information and is scaled uniformly for all plots (as shown on the right in units of $k_B T$). The last cluster in each plot contains amino acids that do not share MI with each other or other clusters, which is why the last diagonal element has a value near 0.

⁶V. Ovchinnikov, M. Karplus, and E. Vanden-Eijnden, *J. Chem. Phys.* **134** (2011).
⁷A. C. Pan, D. Sezer, and B. Roux, *J. Phys. Chem. B* **112**, 3432 (2008).
⁸V. Ovchinnikov and M. Karplus, *J. Chem. Phys.* **140**, 175103 (2014).
⁹L. Maragliano, B. Roux, and E. Vanden-Eijnden, *J. Chem. Theory Comput.* **10**, 524 (2014).
¹⁰D. L. D. Caspar and A. Klug, *Cold Spring Harbor Symp. Quant. Biol.* **27**, 1 (1962).
¹¹E. Grahn, T. Moss, C. Helgstrand, K. Fridborg, M. Sundaram, K. Tars, H. Lago, N. J. Stonehouse, D. R. Davis, P. G. Stockley, and L. Liljas, *RNA* **7**, 1616 (2001).
¹²P. G. Stockley, O. Rolfsson, G. S. Thompson, G. Basnak, S. Francese, N. J. Stonehouse, S. W. Homans, and A. E. Ashcroft, *J. Mol. Biol.* **369**, 541 (2007).
¹³E. C. Dykeman and R. Twarock, *Phys. Rev. E* **81**, 031908 (2010).
¹⁴K. M. ElSawy, L. S. D. Caves, and R. Twarock, *J. Mol. Biol.* **400**, 935 (2010).
¹⁵V. L. Morton, E. C. Dykeman, N. J. Stonehouse, A. E. Ashcroft, R. Twarock, and P. G. Stockley, *J. Mol. Biol.* **401**, 298 (2010).
¹⁶J. Gott, T. Pan, K. Lecuyer, and O. Uhlenbeck, *Biochemistry* **32**, 13399 (1993).
¹⁷P. G. Stockley, N. J. Stonehouse, J. B. Murry, S. T. S. Goodman, S. J. Talbot, C. J. Adams, L. Liljas, and K. Valegard, *Nucleic Acids Res.* **23**, 2512 (1995).
¹⁸E. C. Dykeman, N. E. Grayson, K. Toropova, N. A. Ranson, P. G. Stockley, and R. Twarock, *J. Mol. Biol.* **408**, 399 (2011).
¹⁹S. L. Seyler and O. Beckstein, *Mol. Simulat.* **40**, 855 (2014).
²⁰K. Arora and C. L. Brooks, *Proc. Natl. Acad. Sci. USA* **104**, 18496 (2007).
²¹S. Lu, W. Huang, and J. Zhang, *Drug Discovery Today* **19**, 1595 (2014).

²²Y. Matsunaga, H. Fujisaki, T. Terada, T. Furuta, K. Moritsugu, and A. Kidera, *PLoS Comput. Biol.* **8**, e1002555 (2012).
²³Y. Wang, A. D. Hollingsworth, S. K. Yang, S. Patel, D. J. Pine, and M. Weck, *J. Am. Chem. Soc.* **135**, 14064 (2013).
²⁴H. Hill, N. J. Stonehouse, S. A. Fonseca, and P. G. Stockley, *J. Mol. Biol.* **266**, 1 (1997).
²⁵N. J. Stonehouse, K. Valegård, R. Golmohammadi, S. van den Worm, C. Walton, P. G. Stockley, and L. Liljas, *J. Mol. Biol.* **256**, 330 (1996).
²⁶W. Humphrey, A. Dalke, and K. Schulten, *J. Mol. Graph.* **14**, 33 (1996).
²⁷B. R. Brooks, C. L. Brooks, III, A. D. Mackerell, Jr., L. Nilsson, R. J. Petrella, B. Roux, Y. Won, G. Archontis, C. Bartels, S. Boresch, A. Caffisch, L. Caves, Q. Cui, A. R. Dinner, M. Feig, S. Fischer, J. Gao, M. Hodoscek, W. Im, K. Kuczera, T. Lazaridis, J. Ma, V. Ovchinnikov, E. Paci, R. W. Pastor, C. B. Post, J. Z. Pu, M. Schaefer, B. Tidor, R. M. Venable, H. L. Woodcock, X. Wu, W. Yang, D. M. York, and M. Karplus, *J. Comput. Chem.* (2009).
²⁸D. Van Der Spoel, E. Lindahl, B. Hess, G. Groenhof, A. E. Mark, and H. J. C. Berendsen, *J. Comp. Chem.* **26**, 1701 (2005).
²⁹M. Bonomi, D. Branduardi, G. Bussi, C. Camilloni, D. Provasi, P. Raiteri, D. Donadio, F. Marinelli, F. Pietrucci, and R. a. Broglia, *Comp. Phys. Comm.* **180**, 1961 (2009).
³⁰A. D. J. Mackerell, D. Bashford, M. Bellott, R. L. J. Dunbrack, J. D. Evaseck, M. J. Field, S. Fischer, J. Gao, H. Guo, S. Ha, D. Joseph-McCarthy, L. Kuchnir, K. Kuczera, F. T. K. Lau, C. Mattos, S. Michnick, T. Ngo, D. T. Nguyen, B. Prodhom, W. E. I. Reiher, B. Roux, M. Schlenkrich, J. C. Smith, R. Stote, J. Straub, M. Watanabe, J. Wiorcikiewicz-Kuczera, D. Yin, and M. Karplus, *J. Phys. Chem. B* **102**, 3586 (1998).
³¹A. D. Mackerell, *J. Comput. Chem.* **25**, 1584 (2004).
³²W. L. Jorgensen, J. Chandrasekhar, J. D. Madura, R. W. Impey, and M. L. Klein, *J. Chem. Phys.* **79**, 926 (1983).
³³D. J. Price and C. L. Brooks, *J. Chem. Phys.* **121**, 10096 (2004).
³⁴B. Hess, H. Bekker, H. J. C. Berendsen, and J. G. E. M. Fraaije, *J. Comput. Chem.* **18**, 1463 (1997).
³⁵M. Parrinello and A. Rahman, *J. Appl. Phys.* **52**, 7182 (1981).
³⁶S. Nose and M. L. Klein, *Mol. Phys.* **50**, 1055 (1983).
³⁷U. Essmann, L. Perera, M. L. Berkowitz, T. Darden, H. Lee, and L. G. Pedersen, *J. Chem. Phys.* **103**, 8577 (1995).
³⁸M. A. Rohrdanz, W. Zheng, and C. Clementi, in *Annu. Rev. Phys. Chem., Annu. Rev. Phys. Chem., Vol. 64 (Annual Reviews, 2013)* pp. 295–316.
³⁹A. Dickson and A. R. Dinner, *Annu. Rev. Phys. Chem.* **61**, 441 (2010).
⁴⁰P. G. Bolhuis, D. Chandler, C. Dellago, and P. L. Geissler, *Annu. Rev. Phys. Chem.* **53**, 291 (2002).
⁴¹S. Fischer, K. W. Olsen, K. Nam, and M. Karplus, *Proc. Natl. Acad. Sci. USA* **108**, 5608 (2011).
⁴²R. Elber, *Biophys. J.* **92**, L85 (2007).
⁴³F. Pietrucci, F. Marinelli, P. Carloni, and A. Laio, *J. Am. Chem. Soc.* **131**, 11811 (2009).
⁴⁴M. Lei, M. I. Zavodszky, L. A. Kuhn, and M. F. Thorpe, *J. Comput. Chem.* **25**, 1133 (2004).
⁴⁵D. Moroni, P. G. Bolhuis, and T. S. van Erp, *J. Chem. Phys.* **120**, 4055 (2004).
⁴⁶R. J. Allen, P. B. Warren, and P. R. ten Wolde, *Phys. Rev. Lett.* **94** (2005).
⁴⁷J. Pfaendtner, D. Branduardi, M. Parrinello, T. D. Pollard, and G. A. Voth, *Proc. Natl. Acad. Sci. USA* **106**, 12723 (2009).
⁴⁸A. Barducci, M. Bonomi, and M. Parrinello, *Biophys. J.* **98**, L44 (2010).
⁴⁹B. W. Zhang, D. Jasnow, and D. M. Zuckerman, *Proc. Natl. Acad. Sci. USA* **104**, 18043 (2007).
⁵⁰G. A. Huber and S. Kim, *Biophys. J.* **70**, 97 (1996).
⁵¹A. L. Ferguson, A. Z. Panagiotopoulos, I. G. Kevrekidis, and P. G. Debenedetti, *Chem. Phys. Lett.* **509**, 1 (2011).
⁵²T. S. Van Erp, “Dynamical rare event simulation techniques for equilibrium and nonequilibrium systems,” (John Wiley & Sons,

- Inc., 2012) pp. 27–60.
- ⁵³G. R. Bowman, V. A. Voelz, and V. S. Pande, *J. Am. Chem. Soc.* **133**, 664 (2011).
- ⁵⁴F. Noe, C. Schutte, E. Vanden-Eijnden, L. Reich, and T. R. Weikl, *Proc. Natl. Acad. Sci. USA* **106**, 19011 (2009).
- ⁵⁵J. J. Lacroix, S. A. Pless, L. Maragliano, F. V. Campos, J. D. Galpin, C. A. Ahern, B. Roux, and F. Bezanilla, *J. Gen. Physiol.* **140**, 635 (2012).
- ⁵⁶C. Zhao and S. Y. Noskov, *Plos Comput. Biol.* **9**, e1003296 (2013).
- ⁵⁷J. Schlitter, M. Engels, and P. Kruger, *J. Mol. Graph.* **12**, 84 (1994).
- ⁵⁸C. L. McClendon, G. Friedland, D. L. Mobley, and M. P. Jacobson, *J. Chem. Theory Comput.* **5**, 2486 (2009).
- ⁵⁹R. Golmohammadi, K. Fridborg, M. Bundule, K. Vægård, and L. Liljas, *Structure* **4**, 543 (1996).
- ⁶⁰S. H. E. van den Worm, N. J. Stonehouse, K. Vægård, J. B. Murray, C. Walton, K. Fridborg, P. G. Stockley, and L. Liljas, *Nucleic Acids Res.* **26**, 1345 (1998).
- ⁶¹F. Pontiggia, D. Pachov, M. Clarkson, J. Villali, M. Hagan, V. S. Pande, and D. Kern, submitted (2015).
- ⁶²D. Branduardi and J. D. Faraldo-Gomez, *J. Chem. Theory Comput.* **9**, 4140 (2013).
- ⁶³A. Grossfield, “Wham: the weighted histogram analysis method, version 2.0.9,”.
- ⁶⁴U. von Luxburg, *Stat. Comput.* **17**, 395 (2007).